Supporting Information

Plümper et al. 10.1073/pnas.1612147114

SI Raman Spectroscopy

Raman spectra of organic matter were collected using a Kaiser HoloLab Series 5000 equipped with a diode-pumped solid-state laser (785 nm) (Utrecht University). Hyperspectral mapping was performed with a Horiba Scientific LabRam HR800 (Steinmann Institute, University of Bonn). Raman scattering was excited with a diode-pumped solid-state laser (784 nm) with less than 40 mW at the sample surface. A 100× objective with a numerical aperture of 0.9 was used resulting in a diffraction-limited lateral resolution of ∼1 μm. The confocal hole was set to 1,000 μm, resulting in a depth resolution of a few micrometers. The scattered Raman light was collected in a 180° backscattering geometry by an electron-multiplier charged coupled device detector after passing through a 100-μm (single measurements) or 200-μm (mapping) spectrometer entrance slit and being dispersed by a grating of 600 grooves per millimeter, yielding a spectral resolution of 1.7 and 2.3 cm^{-1}, respectively, as determined from the width of Ne lines. The spectrometer was calibrated with the first-order Si Raman band at 520.7 cm^{-1} and Ne lines. The total acquisition time varied between 900 and 1,200 s for single measurements and 25 × 0.5 s for mapping. Normalization of Raman spectrum to the most intense epoxy band at 815 cm^{-1} shows no contribution of bands from the epoxy resin (Fig. S1). This is evident by the absence of epoxy bands (arrow in Fig. S1) between 950 and 1,000 cm^{-1} in the sample spectra. The false-color Raman image shown in Fig. 2*G* is generated from the spectra recorded for each pixel of the image by color-coding the ratio between the integrated intensity of an organic vibrational modes near 639 cm^{-1} and a serpentine mode at 690 cm^{-1} (Fig. S2). Warm colors reflect a high content of organic material within the analyzed volume, whereas blue colors mark regions with low or undetectable organic material. Spectra were collected over an area of 60 × 60 μm^2 with a step size of 0.5 μm, resulting in 7,200 spectra. The resulting map is shown in Fig. S4. To obtain reduced or $R(\omega)$ intensities for future comparison that are independent from the instrument, the laboratory temperature, and the excitation wavenumber, ν_e, and thus directly proportional to relative scattering activity, the Raman spectra from the mesh core were also corrected for (*i*) the instrument response function (white light correction); (*ii*) the excitation frequency dependence, that is, by the scattering factor, $(\nu_e - \nu)^3$, with ν being the wavenumber of the scattered light (intensities were measured in photons per second); and (*iii*) the temperature effect, that is, by the Bose–Einstein temperature factor, $1 - \exp(-h\nu c/kT)$, with h, c, k, and T being the Planck constant, the speed of light, the Boltzmann constant, and the temperature, respectively. The corrected spectra were deconvoluted by least-squares fitting Gauss–Lorentz functions along with a linear background that was subtracted after the least-squares fit (Fig. S5 and Table S1). The error of the reported band positions is smaller than 0.1 cm^{-1}. Raman evaluation of the serpentine polymorphs present in the rim and core structures was conducted by examining the water vibration region at ∼3,600 cm^{-1}. Raman spectra taken, using the 785-nm laser, showed no evidence for the OH bands due to the low scattering efficiency of these bands with this laser. Therefore, the 532-nm coherent compass sapphire laser of a WITec alpha 300R was used for the OH band analysis of serpentine group minerals. The analysis was conducted with a 50× long working distance lens with a 0.55 numerical aperture in backscattering geometry to the sample. After the scattered Raman light passed through a pinhole of 20 μm, the light was dispersed on a grating of 1,800 grooves per millimeter, resulting in a spectral resolution of 1.1 cm^{-1} in the spectral region of interest, measured using a built-in calibration light source.

SI Opaque Mineral Grain Analysis

Fig. S6 shows the distribution of opaque mineral grains (high backscattering intensity in Fig. S6*A*) within the serpentinites clasts. Several FIB-SEM sections were prepared across the mesh rim–core interfaces, where Fig. S6*B* shows a representative high angle annular dark field (HAADF) image highlighting three nanoparticles with high intensity (overview image in main-text Fig. 3*C*). The intensity in an HAADF image scales with atomic number, implying that the nanoparticles are atomically heavier than the surrounding serpentine grains. Energy-dispersive X-ray analysis (Fig. S6*C*) reveals that the nanoparticle exist exclusively of Ni and Fe in a ∼2:1 ratio. Together with chemical analysis conducted on the micrometer-scale in a scanning electron microscope, the microstructural association of the particles within the serpentinites, and the limited possibilities of potential mineral phases with Ni and Fe in a ∼2:1 ratio (65), we conclude that the nanoparticles are awaruite (Ni_2Fe–Ni_3Fe).

SI Estimation of the Maximum Depth for the Current Temperature Limit for Life

A sketch of the one-dimensional steady-state heat conduction model to estimate the maximum depth for the current temperature limit for life in subduction zone forearcs is found in Fig. S7.

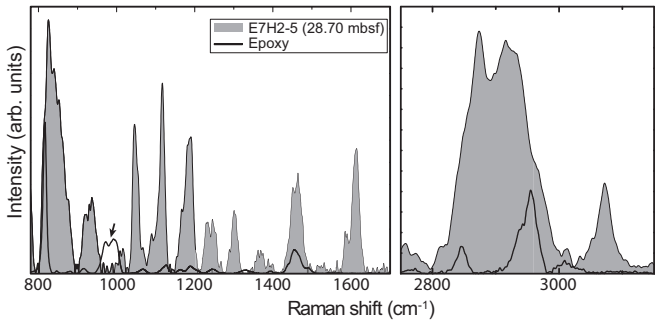

Fig. S1. Epoxy-normalized Raman spectrum of sample E7H2-5 (28.70 mbsf). All spectra were normalized to highest intensity epoxy Raman mode (815 cm^{-1}), showing that epoxy does not contribute to the observed Raman spectra of the identified organic molecules.

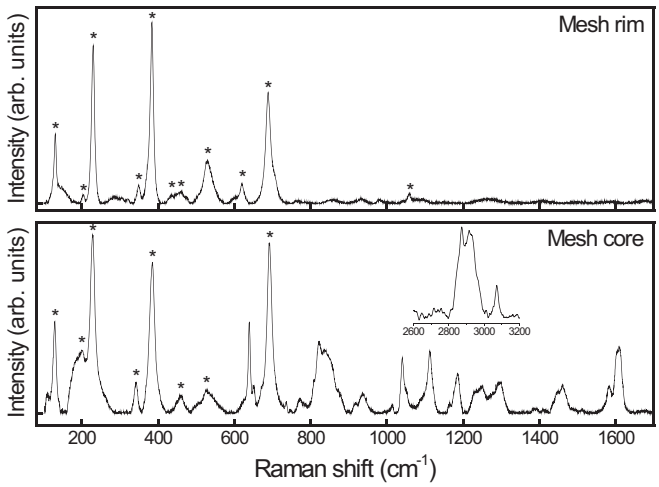

Fig. S2. Representative Raman spectra of the mesh core and rim region taken from the area in which hyperspectral imaging was performed. Bands marked with an asterisk belong to lizardite/chrysotile. All other bands reflect complex organic material (see main text and Table S1).

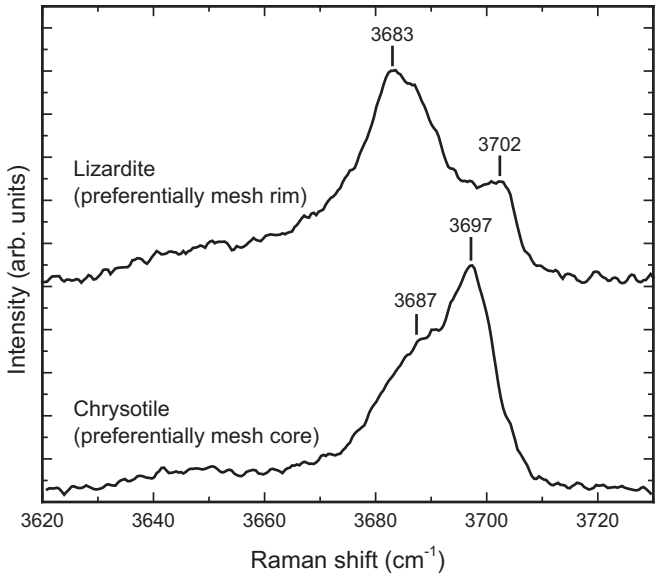

Fig. S3. Representative Raman spectra of OH-stretching modes, fingerprinting lizardite and chrysotile (e.g., ref. 64) typically found in the mesh rim and core regions, respectively, of the serpentinite clasts.

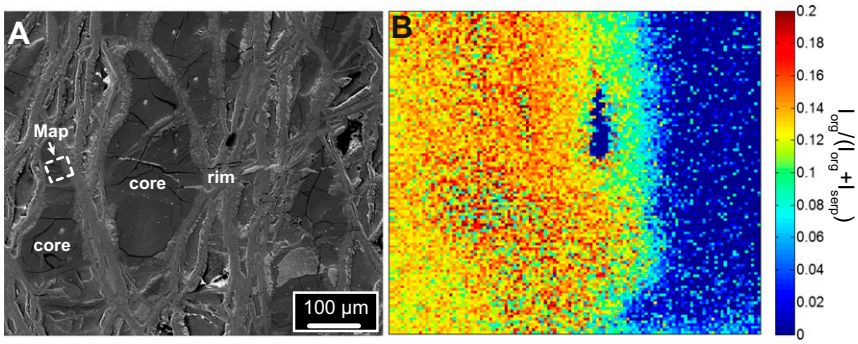

Fig. S4. (*A*) Backscattered electron image showing the location of the Raman map. (*B*) Shown is the distribution of organics within the mesh core and rim. I_{org} and I_{serp} are the integrated intensities of the bands near 639 and 690 cm^{-1}, respectively.

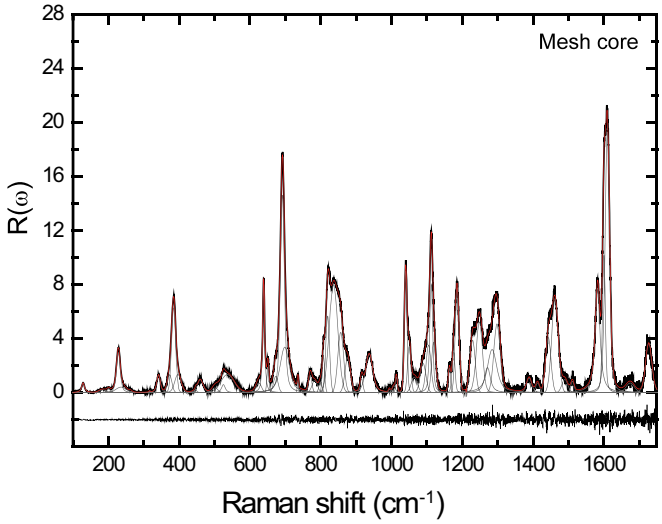

Fig. S5. Raman spectrum as shown in Fig. S2 from the mesh core, but with reduced intensities $R(\omega)$ that were obtained by correcting the measured intensities for the instrumental response function, temperature effects, the excitation frequency dependence, and background (for more details, see *Methods* in the main text). Also shown is the deconvolution of the spectrum obtained from least-squares fitting individual Gauss–Lorentzian functions (gray curves) to the data. The red curve represents the sum curve. The residuals of the fitting procedure are also shown.

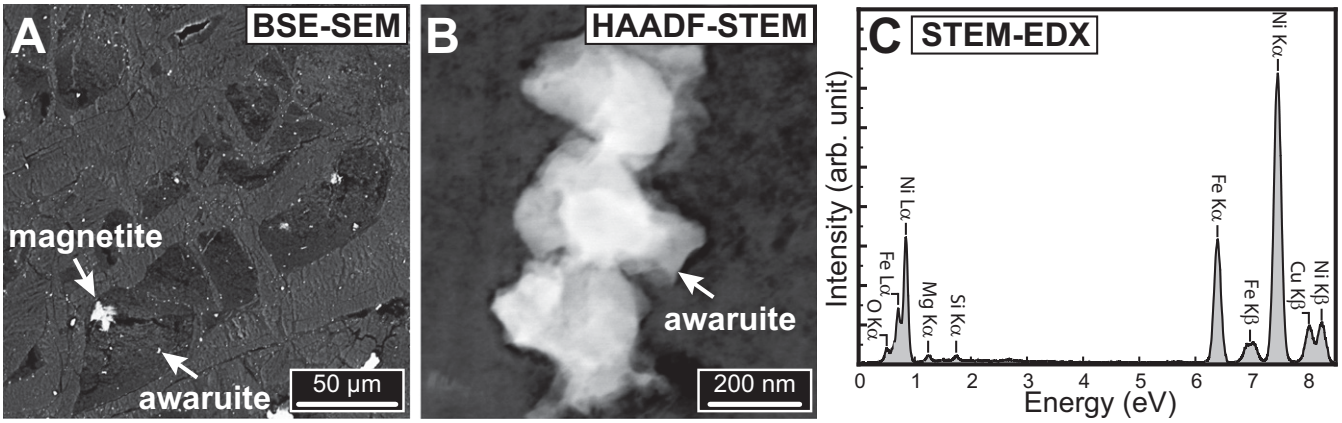

Fig. S6. *A* is a backscattered electron (BSE) image taken in a scanning electron microscope showing the distribution of opaque minerals (high backscattering intensity). *B* is a high-angle annular dark-field (HAADF) image taken with transmission electron microscope in scanning mode. The corresponding EDX analysis of a nanosized awaruite grain is shown in *C*. The Cu Kβ peaks originates from the FIB section sample holder. The Mg Kα, Si Kα, and O Kα peaks are a minor contribution from the surrounding serpentine grains.

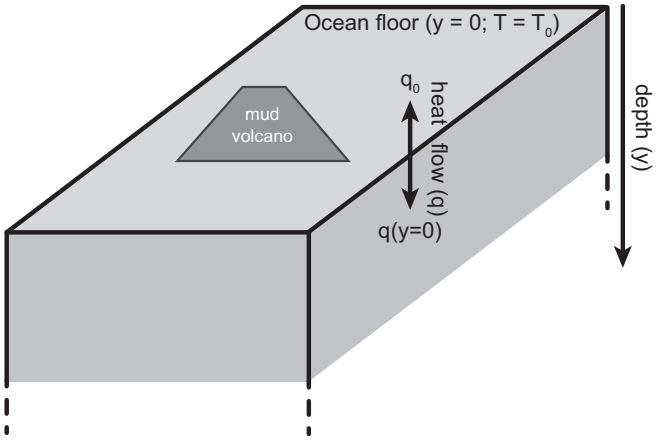

Fig. S7. Sketch of the one-dimensional steady state heat conduction model (modified after ref. 34).

Table S1. Band positions, band widths (FWHM), and relative intensities of Raman bands observed from the mesh core region

Band position, cm^{-1}	Relative intensities	FWHM, cm^{-1}	Assignment	Band position	Relative intensities	FWHM	Assignment
128.4	4	9.9	Liz./Chr.	915.6	5	9.1	
182.8	1	21.8		937.1	15	23.9	
200.5	1	12.1	Liz./Chr.	994.1	1	6.1	
228.1	15	12.6	Liz./Chr.	1,006.9	3	10.9	
236.2	2	35.3		1,014.2	6	5.8	
263.4	0	9.3		1,040.0	47	9.0	N(C–C)
316.3	1	4.9		1,050.2	18	10.0	N(C–C)
341.8	7	11.9	Liz./Chr.	1,064.7	6	20.0	
372.8	7	15.1		1,089.4	11	18.7	
384.3	33	13.5	Liz./Chr.	1,104.8	18	16.2	C–C/C–N/C–O–C
396.4	7	17.0		1,112.4	42	9.7	C–C/C–N/C–O–C
447.0	1	6.5		1,119.2	19	13.7	C–C/C–N/C–O–C
459.7	5	18.9	Liz./Chr.	1,163.9	9	7.9	
501.2	2	19.2		1,175.6	16	9.7	
525.0	3	12.6	Liz./Chr.	1,185.6	40	12.5	C–O str.
536.5	7	44.6		1,229.5	20	16.9	Amide III
625.1	4	17.6		1,248.5	27	20.5	Amide III
639.0	42	6.6	Phenol ring*	1,271.3	10	19.6	Amide III
650.8	9	6.8		1,284.6	17	31.2	Amide III
673.0	6	15.1		1,298.2	26	20.8	Amide III
691.7	76	13.5	Liz./Chr.	1,389.1	6	17.4	
698.4	17	30.5		1,413.0	4	12.8	
735.7	5	4.5		1,443.3	21	17.9	$C–H_2$ def./CH_3
770.2	7	11.1		1,462.2	36	21.7	$C–H_2$ def./CH_3
783.1	5	18.2		1,489.9	5	19.6	
799.4	4	10.2		1,511.6	4	7.9	
807.8	14	8.0		1,582.7	40	15.8	Protein
819.6	29	12.6		1,600.4	53	9.3	Phenol ring*
836.2	41	28.4	Phenol ring*	1,610.3	100	15.2	Phenol ring*
856.5	23	19.2	Phenol ring*	1,674.9	4	27.8	
876.3	13	17.9		1,727.2	19	20.8	

Chr., chrysotile; def., deformation; Liz., lizardite; str., stretching.

*Phenol ring vibration typical for the amino acid tyrosine (63); Raman band assignment of serpentine phases after ref. 64 and organics after refs. 6, 30, and 31.